Multiwavelength flare observations of the blazar S5 1803+784

R. Nesci [1]★ S. Cutini,[2]★ C. Stanghellini,[3]★ F. Martinelli,[4] A. Maselli,[5,6] V. M. Lipunov,[7] V. Kornilov,[7]
R. R. Lopez,[8] A. Siviero,[9] M. Giroletti [3] and M. Orienti[3]

[1]*INAF/IAPS, via Fosso del Cavaliere 100, I-00133 Roma, Italy*
[2]*INFN, Via Alessandro Pascoli, s.n.c, I-06130 Perugia, Italy*
[3]*INAF/IRA, Via P. Gobetti, 101, I-40129 Bologna, Italy*
[4]*Lajatico Astronomical Centre, Via dei Mulini a Vento 9, I-56030, Orciatico (PI), Italy*
[5]*INAF/OAR, Via Frascati 33, I-00078 Monte Porzio Catone (Roma), Italy*
[6]*ASI/SSDC, Via del Politecnico snc, I-00133 Roma, Italy*
[7]*Physics Department, Lomonosov Moscow State University, Sternberg Astronomical Institute, 119991 Moscow, Vorobievy hills, 1, Russia*
[8]*Instituto de Astrofisica de Canarias Via Lactea, s/n, E-38205 La Laguna (Tenerife), Spain*
[9]*Department of Physics and Astronomy, University of Padova, Via Francesco Marzolo 8, I-35122 Padova, Italy*

ABSTRACT

The radio, optical, and γ-ray light curves of the blazar S5 1803+784, from the beginning of the *Fermi*-Large Area Telescope (LAT) mission in 2008 August–2018 December, are presented. The aim of this work is to look for correlations among different wavelengths useful for further theoretical studies. We analysed all the data collected by *Fermi*-LAT for this source, taking into account the presence of nearby sources, and we collected optical data from our own observations and public archive data to build the most complete optical and γ-ray light curve possible. Several γ-ray flares ($F > 2.3\,10^{-7}\mathrm{ph}(E > 0.1\ \mathrm{GeV})\,\mathrm{cm}^{-2}\,\mathrm{s}^{-1}$) with optical coverage were detected, all but one with corresponding optical enhancement; we also found two optical flares without a γ-ray counterpart. We obtained two *Swift* Target of Opportunity observations during the strong flare of 2015. Radio observations performed with VLBA and EVN through our proposals in the years 2016–2020 were analysed to search for morphological changes after the major flares. The optical/γ-ray flux ratio at the flare peak varied for each flare. Very minor optical $V - I$ colour changes were detected during the flares. The X-ray spectrum was well fitted by a power law with photon spectral index $\alpha = 1.5$, nearly independent of the flux level: No clear correlation with the optical or the γ-ray emission was found. The γ-ray spectral shape was well fitted by a power law with average photon index $\alpha = 2.2$. These findings support an inverse-Compton origin for the high-energy emission of the source, nearly co-spatial with the optically emitting region. The radio maps showed two new components originating from the core and moving outwards, with ejection epochs compatible with the dates of the two largest γ-ray flares.

Key words: BL Lacertae objects: individual – galaxies: jets – quasars: emission lines – gamma-rays: galaxies – X-rays: galaxies.

1 INTRODUCTION

BL Lacertae objects are a subclass of active galactic nuclei (AGN) characterized by fast and large flux variations. Their emission ranges from radio frequencies up to γ-rays, and their spectral energy distribution (SED) in a $\mathrm{Log}(\nu)$ *versus* $\mathrm{Log}(\nu \times F_\nu)$ plane may be described by a double bell shape: the first peak is located between the far-infrared and X-ray frequencies, while the second one is always at much higher energies (from X-ray to γ-ray energies). A current interpretation of this double bell shape is that synchrotron radiation from relativistic electrons in a highly collimated jet is responsible for the low-frequency peak, while inverse-Compton radiation from these electrons impacting local photons produces the higher frequency peak. This model is likely an oversimplification

with respect to reality: The black hole at the centre of the host galaxy is surrounded by an accretion disc, a hot corona, and the relativistic jet approximately directed along the black hole rotation axis is likely structured at least in an inner part (spine) and an outer envelope (sheath) with different physical conditions (Chiaberge et al. 2000). Such a differentiated structure implies that the radiation at different frequencies may come from physically different spatial regions: flux variations at different frequencies may therefore reach the observer at different times. Thus multiwavelength simultaneous observations are an efficient tool to explore the physical structure of the emitting regions.

This paper is an observational contribution to the study of S5 1803+784, a radio-selected BL Lac object (Biermann et al. 1981) at $z = 0.683$ (Lawrence et al. 1996); a detailed modelling of the emission processes and morphology is beyond the scope of this paper. S5 1803+784 is characterized by large variations in the optical range (Nesci et al. 2002, 2012) and is well detected at γ-ray energies by the *Fermi*-Large Area Telescope (LAT; Atwood et al. 2009), from the

first LAT Catalogue of AGN (Abdo et al. 2009), up to the most recent one (Ajello et al. 2020). In the taxonomical classification scheme of BL Lac objects by Padovani & Giommi (1995), the source is low synchrotron peaked (LSP), with the synchrotron emission peaked around 10^{13} Hz: This is clearly shown by its broad-band SED (Nesci et al. 2002).

In this paper, we present the light curves of the source in the radio (15 GHz), optical (R_C), and γ-ray bands from year 2008 to 2018, with snapshots in the X-ray and optical bands by the *Neil Gehrels Swift Observatory* X-ray Telescope (XRT) and the UltraViolet and Optical Telescope (UVOT), to search for correlations among different wavelengths. Furthermore, we present Very Long Baseline Interferometry (VLBI) radio observations performed after two large flares, to look for morphological changes in its inner jet structure.

2 OBSERVATIONAL DATA

2.1 Optical photometry

We have been monitoring this source in the optical band since 1996 (Nesci et al. 2002, 2012) despite with some large gaps. It was serendipitously observed by the MASTER robotic network (Lipunov et al. 2010) since 2010. Due to its very northern position in the sky, it was not covered by the Catalina Sky Survey (Drake et al. 2009); since 2011 July, this source became a target of the blazar monitoring program by the KAIT telescope (Li et al. 2003).

In this paper, we used our observations taken with several telescopes since 2009: the 50-cm *F*/4.5 at Vallinfreda, the 30-cm *F*/4.5 at Greve in Chianti, the 1.5-m telescope at the Loiano Observatory, the 23-cm *F*/10 of the Department of Physics of La Sapienza University, and the 50-cm *F*/4.4 at the Lajatico Astronomical Centre. All these telescopes are equipped with CCD cameras and Cousins *R* filters. Magnitudes were derived using aperture photometry with IRAF/APPHOT,[1] using always the same comparison sequence (Nesci et al. 2002).

In past years (Nesci et al. 2002, 2012), the colour indexes ($V - R$ and $R - I$) of the source showed only small variations, with a mild bluer-when-brighter behaviour. This is also shown by the present data set (see Table 1, from which we derive an average increase of 0.04 mag in $R - I$ for a 1-mag increase in R), and makes us confident of the reliability of converting V magnitudes into R ones with a fixed colour index for the purpose of building a denser historical light curve. Therefore we included in our data set the V magnitudes from the 30-cm *F*/10 telescope of the Foligno Observatory and from the 40-cm *F*/8 telescope of the Royal Observatory of Belgium (Lampens & van Cauteren 2015), converting their V magnitudes into R_C, adopting $V - R = 0.50$ mag. For the KAIT observations, which are unfiltered and use the USNO-B1 (Monet et al. 2003) R2 magnitudes as reference, we applied an average correction of -0.20 mag to their psf magnitudes, based on the average offset of our photometric sequence stars with respect to the USNO-B1 catalogue: This value is within the quoted systematic uncertainty given in the KAIT data base. For the MASTER observations, which are also unfiltered and expressed as a nearly R_C magnitude, we verified a good consistency with our magnitudes for the few nights of simultaneous observations. The resulting overall R_C light curve is shown in the middle panel of Fig. 1.

Table 1. Optical colours from la Lajatico (LA) and Loiano (LO) Observatories multifilter observations.

Date	Date (MJD)	R (mag)	$V - R$ (mag)	$R - I$ (mag)	$V - I$ (mag)	Tel
2011-07-21	55763.84	15.85	0.49	0.70	1.19	LO
2011-07-22	55764.83	15.88	0.50	0.70	1.20	LO
2015-08-21	57255.85	14.19	0.49	0.59	1.08	LA
2015-08-26	57260.82	13.91	0.50	0.59	1.09	LA
2015-08-28	57262.84	13.76	0.51	0.64	1.15	LA
2015-08-31	57265.86	13.97	0.46	0.61	1.07	LA
2015-09-05	57270.86	14.66	0.48	0.68	1.16	LA
2015-09-09	57274.84	14.55	0.48	0.68	1.16	LA
2015-09-19	57284.87	14.30	0.53	0.65	1.18	LA
2015-09-21	57286.81	14.58	0.48	0.69	1.17	LA
2015-10-11	57306.81	15.02	0.45	0.68	1.13	LA
2015-10-22	57317.75	15.75	0.51	0.71	1.22	LA
2015-11-24	57350.74	14.23	0.50	0.62	1.12	LA
2016-05-21	57729.92	15.97	0.49	0.69	1.18	LA
2016-06-26	57565.07	15.29	0.49	0.78	1.27	LA
2016-07-01	57570.07	15.48	0.61	0.63	1.24	LA
2016-07-09	57578.92	16.33	0.35	0.66	1.01	LA
2016-12-15	57737.80	15.13	0.49	0.00	0.00	LA
2016-12-29	57751.78	15.77	0.46	0.00	0.00	LA

Note. Date in Column 1, R_C in column 2, $V - R_C$ in column 3, $R_C - I_C$ in column 4, $V - I_C$ in column 5, and Observatory in column 6.

This light curve shows a baseline flux level between 1 and 2 mJy, with several flares, and some short time intervals with flux below 1 mJy.

The definition of flare is somewhat arbitrary, since it depends on the assumed quiescent level of the source. From the optical light curve, we derived an average quiescent level of 1.5 mJy ($R = 16.0$ mag), and we considered a flare as a rise and fall episode in the light curve with a peak value higher than 3 mJy ($R = 15.2$ mag). For the better sampled flares, we measured the duration and the slopes of the rising and falling branches. The duration was defined as the time interval during which the source was above the average level ($R_C = 16.0$ mag): The uncertainties of these intervals depend on the sampling of the light curve. The slopes (mag d^{-1}) were derived with a linear fit to the manually selected relevant data. A total of 11 flares were identified in this way and are listed in Table 2. The simultaneous presence of a γ-ray flare (see Section 2.3 below) is given in the last column.

2.2 Optical spectroscopy

Only three spectra of this source have been published so far: one taken in 1987 (Lawrence et al. 1996) showing the Mg II 2790-Å emission line with equivalent width (EW) = 8.8 Å; one taken in 1996 (Rector & Stocke 2001) that reports for the Mg II line an EW = 2.8 Å; the last taken in 2018 (Paiano et al. 2020) with EW = 8.3 Å, very similar to the value of 1987. The magnitude of the source in 1987 is unknown, while from our monitoring, we know that it was faint in 1996 ($R = 16.2$ mag), as well as in 2018 ($R = 15.9$ mag).

We obtained a spectrum of the source on 2015 August 27 (MJD 57261), when it was near the maximum level ($R = 13.8$ mag), with the 1.22-m telescope of the Asiago Observatory equipped with an Andor iDus DU440 camera and a Boller & Chivens spectrograph with a 300 gr mm^{-1} grating: The dispersion was 2.3 Å pixel^{-1} and the spectral resolution 9.5 Å, derived from the full width at half-maximum of the night-sky emission lines. Wavelength calibration was made with an He-Fe-Ar lamp and instrumental response calibration with the star
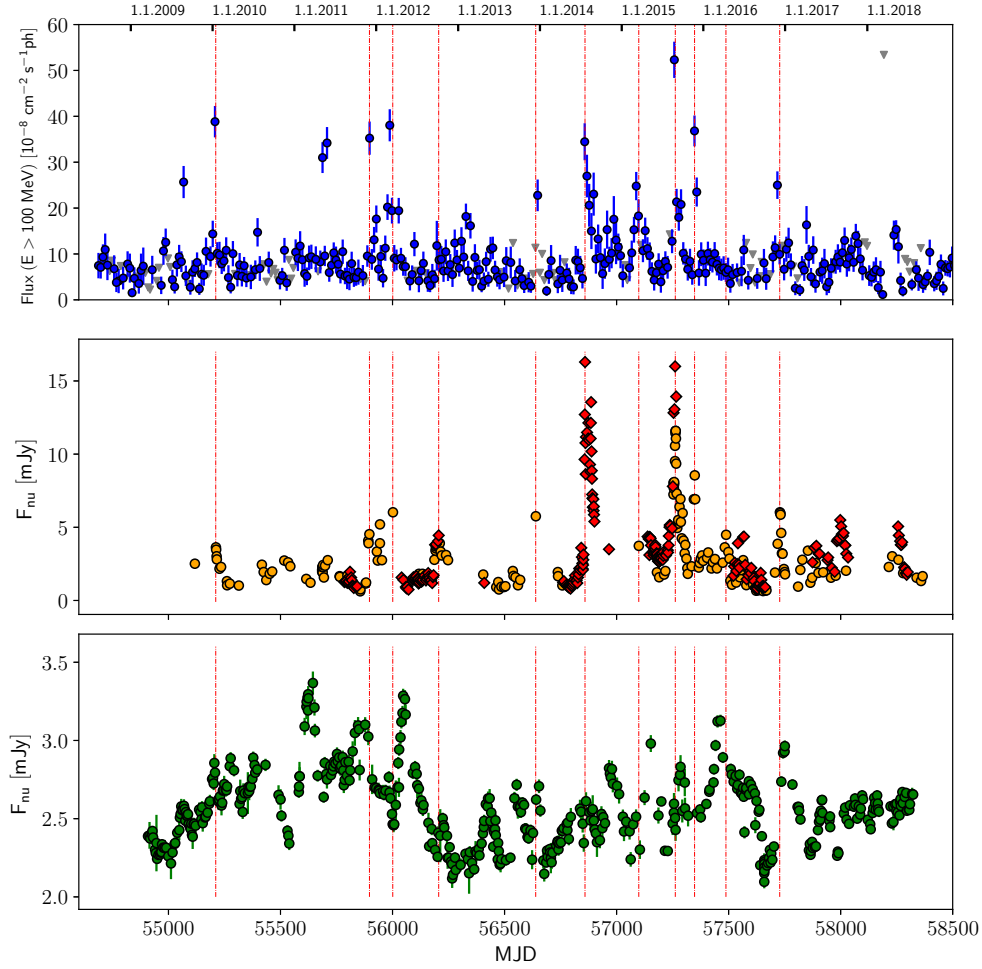
Figure 1. The combined light curve of S5 1803+784 in linear scale: lower scale in MJD, upper scale in calendar years. Upper panel, γ-ray, binned at 10-d intervals: Blue points are detections, grey triangles are upper limits. Middle panel, optical: Orange points are our own data, red points are KAIT public data. Lower panel: radio 15 GHz from OVRO monitoring. Vertical lines mark the flares discussed in the text.

Table 2. Optical flares data: date of the maximum (column 1), the peak R_C magnitude (column 2), the flare duration (column 3), the slope of the rising (column 4), and of the dimming branch (column 5).

Date (MJD)	Peak R_C (mag)	Duration (d)	Rising (mag d^{-1})	Falling (mag d^{-1})	γ flare
55211	15.0	45		0.07	Yes
55897	14.7				Yes
56001	14.4				Yes
56206	14.5	60	0.076		No
56639	14.5				Yes
56859	13.9	45	0.22		Yes
57099	15.0				Yes
57262	13.7		0.11		Yes
57348	14.0				Yes
57488	14.8				No
57728	14.4	30	0.08	0.10	Yes

HR 7596. The blazar spectrum in arbitrary flux units is shown in Fig. 2.

The S/N ratio was about 20, allowing the detection of an emission line of EW = 3 Å. No such line was present at 4710 Å, the expected position of the Mg II line, and the spectrum showed no features besides the telluric ones. The spectral slope was fully consistent with that derived from our VRI photometry.

2.3 *Fermi*-LAT data analysis

The data analysis was performed following the *Fermi*-LAT collaboration recommendations for point-source analysis[2] and is briefly described as follows. We built the historical light curve collecting almost 10 yr of data available from the *Fermi*-LAT archive, starting from 2008 August 4 up to 2018 December 31. We analysed the *Fermi*-LAT data using the FERMITOOLS package version 1.2.1 available from the Fermi Science Support Center (FSSC)[3] through the Conda package manager hosted on GitHub[4] and the P8R3_SOURCE_V2 instrument response functions (Atwood et al. 2013). We selected a Region of Interest (ROI) with a radius of 15° centred at the position of S5 1803+784 and we used only events belonging to the 'source' class. The binned maximum likelihood was performed using as background model the 4FGL sources lying in an ROI with a radius

[2]https://fermi.gsfc.nasa.gov/ssc/data/analysis/documentation/
Pass8_usage.html.

[3]https://fermi.gsfc.nasa.gov/ssc/.

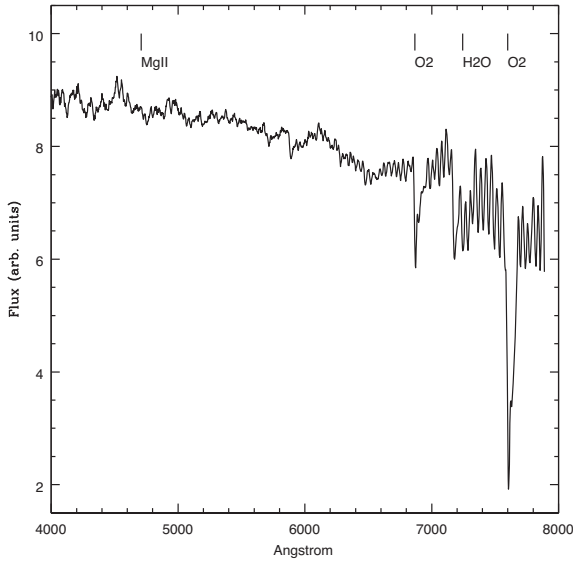[4]https://github.com/fermi-lat/Fermitools-conda/.

Figure 2. The spectrum of S5 1803+784 from the Asiago Observatory, corrected for instrumental response and smoothed with a running mean of 7 pixels, in arbitrary flux units. Telluric oxygen (O_2) and water absorption bands (H_2O) are well evident; the expected position of the Mg II emission is also marked. The apparent emission around 4525 Å is a residual from night-sky emission lines.

of $20°$ (4FGL; Abdollahi et al. 2020) and the isotropic and Galactic diffuse emission components (iso_P8R3_SOURCE_V2_v1.txt and gll_iem_v07.fits,[5] respectively). We fixed the spectral indexes of background sources to the 4FGL values, but the fluxes of sources within a radius of $10°$ from the source of interest were left free to vary. Light curves were derived by dividing the data in bins of 10-d duration for the historical and 1- and 3-d bins for the flaring epochs. We defined as flaring state a flux above 100 MeV larger than 2.3×10^{-7} ph cm^{-2} s^{-1} in a 10-d bin, three times the average value of fluxes in the 10-d light curve. Each bin of the light curves and of the spectra was obtained using a power-law model for the source of interest. For each bin, we extracted the test statistic (TS; Mattox et al. 1996) defined as: $TS = -2(lnL_0 - lnL_1)$ where L_0 is the value of the likelihood calculated in the null hypothesis (no point source in ROI) and L_1 is the value of the likelihood when the source of interest is included (after parameter optimization). We calculated the upper limit (UL) at 2σ confidence level using the Bayesian computation (Helene 1983) and integrated UL when the TS < 1 and TS < 4 respectively, the number of predicted photons $N_{pred} < 3$, or the percentage error on the flux greater than 50 per cent. The light curve in the 0.1–300 GeV range, binned at 10-d intervals, is shown in the upper panel of Fig. 1: The light curve shows a flat, oscillating behaviour with a typical flux level of 0.75×10^{-7} photons cm^{-2} s^{-1} and several large flares, irregularly spaced, listed in Table 3. The flux in the largest flares was nearly 10 times higher than the quiescent state. Thanks to the regular monitoring of the satellite, for all the γ-ray flares, it was possible to measure a duration, which ranges between 20 and 90 d, with an uncertainty of 3 d. In Table 3, we report the γ-ray flare details.

Table 3. γ-ray flare data: the MJD of the peak emission (column 1), the peak flux value (column 2), the flare duration (column 3), the corresponding optical flux (column 4), and the optical/ γ-ray flux ratio (column 5, $\times 10^7$).

Date	Peak flux (photons cm^{-2} s^{-1})	Duration	R_C	Opt/gamma-ray
(MJD)		(d)	(mJy)	
55067	2.6×10^{-7}	40	–	–
55207	4.0×10^{-7}	60	3.6	0.90
55707	3.5×10^{-7}	80	2.7	0.77
55897	3.8×10^{-7}	90	4.5	1.18
55987	3.6×10^{-7}	40	6.0	1.66
56647	2.3×10^{-7}	20	5.7	2.48
56857	3.6×10^{-7}	60	12.3	3.41
57257	5.0×10^{-7}	40	11.6	2.32
57347	3.7×10^{-7}	30	8.5	2.30
57717	2.5×10^{-7}	20	6.0	2.40

2.4 X-ray and ultraviolet photometry

We used X-ray data from the XRT on board the *Neil Gehrels Swift Observatory* (Gehrels et al. 2004), retrieved from the *Swift* archive and acquired from 2009 to 2015; these include data corresponding to the 2015 August flare, respectively 5 d before and 11 d after the the optical maximum. All data were processed with the XRTDAS software package (v.3.6.0), developed at the Space Science Data Center (SSDC) of the Italian Space Agency (ASI) and distributed within the HEASOFT package (v.6.28) by the NASA High Energy Astrophysics Archive Research Center (HEASARC). All the XRT observations were carried out in the most sensitive photon counting (PC) readout mode. Event files were calibrated and cleaned applying standard filtering criteria with the XRTPIPELINE task and using the latest calibration files available in the *Swift* CALDB distributed by HEASARC. Events in the energy range 0.3–10 keV with grades 0–12 were used in the analysis, and the exposure maps were also created with XRTPIPELINE. Source detection was carried out using the detection algorithm DETECT within XIMAGE, also providing the count rate corrected for psf, vignetting, and exposure.

For each observation, source events were extracted from a circle with a radius of 20 pixels centred at the source coordinates; a concentric annulus with radii of 50 and 80 pixels was used for the background. These region files were then used as input to the XRTPRODUCTS task to obtain high-level scientific products: Among these, the spectrum and ancillary files were used to perform a spectral analysis with XSPEC (v.12.11.1). We fitted these spectra using a power-law model, fixing the absorption at the Galactic value ($n_H = 3.4\ 10^{20}$ cm^{-2}), and we computed the flux in the 0.3–10 keV band with its 1σ error.

To compare the X-ray and optical luminosity, we looked at the *Swift*-UVOT simultaneous observations. Aperture photometry of the UVOT images was made with the UVOT online analysis tool available from the SSDC (uvotimgqlprocver v1.14). The source radius was 5 arcsec and the sky level was evaluated within a concentric corona between 27 and 35 arcsec distant from the source. Unfortunately, only in four pointings were all six UVOT filters used, but we found that the optical spectral slope was substantially constant (-0.57 ± 0.03 in the log(ν) versus log($\nu\ F(\nu)$) plane), and therefore we could compute by extrapolation the corresponding R_C magnitudes for all the UVOT pointings. In some cases, we also had nearly simultaneous R_C observations from the ground, confirming the reliability of our extrapolation procedure within 0.2 mag.

Our results from the analysis of the Gehrels et al. (2004) data are reported in Table 4. The last column is the corresponding R_C magnitude. Observations with relatively poor exposure are also reported. Overall, the XRT fluxes changed by a factor of ∼2, and the spectral slope had an average value of 1.51 ± 0.13, with only marginal evidence (correlation coefficient $r = -0.54$) of hardening at higher fluxes.

3 RADIO OBSERVATIONS

To explore if the strong flares of the years 2014 and 2015 produced detectable changes in the structure of the inner part of the source, we obtained radio images of the core of S5 1803+784 at sub-milliarcsecond resolution. Our observations were performed with the Very Long Baseline Array (VLBA) and the European VLBI Network (EVN) at 15, 22, and 43 GHz in six epochs, spanning from 2016 June to 2018 March, as listed in Table 5. We also collected radio data at 15 GHz from the 40-m Telescope of the Owens Valley Radio Observatory (OVRO; Richards et al. 2011) public archive to explore the possibility of activity simultaneous to the optical and γ-ray flares. The radio data are shown in the bottom panel of Fig. 1. We did not find any obvious evidence of correlations.

3.1 Data reduction

Amplitude and phase calibration of the VLBA data were carried out with the AIPS data reduction package in a standard way following the guidelines given in appendix C of the AIPS cookbook: the typical flux error was 5 per cent. Data from the third VLBA epoch were of lower quality especially at 43 GHz, maybe for bad weather conditions at some antennas. A-priori calibration of antenna gains proved to be infeasible for EVN data, and we could not obtain reliable flux density values. We relied on several iterations of imaging and self-calibration (amplitudes and phases) to obtain the relative position of the components. Model fitting of the visibilities was performed with the task MODELFIT available in the Caltech software package DIFMAP.

The morphological radio structure of S5 1803+784 at milliarcsecond (mas) scale can be described as a diffuse emission from an opening jet, directed east–west, with knots and brightness enhancements in several locations along the jet (see e.g. Roland et al. 2008 and references therein). Evidence in support of a helical jet has been presented by Britzen et al. (2010) and Kun et al. (2018) from a long-term monitoring at different frequencies.

This complex structure makes it difficult to compare observations at different epochs observed with different baseline distributions, thus different angular resolution and different sensitivity to diffuse emission. In particular, our 2016 observations were made with the full VLBA array (10 antennas), while in the 2017 sessions, two antennas were missing (Los Alamos and Pie Town in March, St. Croix and Pie Town in November). To have consistency in the components found with MODELFIT, it is important to minimize the effect of the different baseline distributions, especially at the lowest frequency where the detection of the diffuse emission is more relevant. Therefore, at 15 GHz, solely for the MODELFIT procedure, the UV planes of the data were matched as much as possible, excluding two antennas from the 2016 data sets and cutting as needed the inner baselines.

VLBA additional data at 15 GHz (seven epochs) from the MO-JAVE project (Lister et al. 2018) on 2019 and 2020 were added to the analysis. The typical UV coverage of the MOJAVE data was significantly different from ours, and generally better. Calibrated visibilities were downloaded from the MOJAVE archive, imaged and model fitted again in AIPS and DIFMAP.

3.2 Morphological analysis

In Fig. 3, we show our VLBA map at 15 GHz taken on 2016 September 4, while in Fig. 4, we show our map at 43 GHz, which has a higher resolution. Fig. 5 was built by us reprocessing all the public MOJAVE data at 15 GHz of the years 2019–2020, stacking the seven images together, and shows the source morphology at a larger scale.

Given the morphology of this radio source, the attempt to describe the parsec-scale emission with a limited number of discrete components gives a rough approximation of the real structure. Furthermore, the choice of the number of components to describe the source is not trivial, especially when trying to compare the structure at various epochs. Additional caution is needed to compare the morphology at different frequencies, as different angular resolution, different sensitivity to diffuse emission, and different intrinsic opacity may introduce shifts in the positions and delays in the estimated proper motion.

We decided to describe the radio source with a minimum number of Gaussian components. Besides the core, we identified a component A, very close to the core, which is detected only at 22 and 43 GHz in our data, but is well detected in the 15-GHz MOJAVE data taken 4 yr later; a component B, detected at all frequencies, definitely moving outwards, and a component C, apparently steady. Both B and C components were required to fit the MOJAVE 2020 data: Our C component corresponds to the Ca component in the Kun et al. (2018) and Roland et al. (2008) nomenclature. The uncertainty on our component positions is ∼0.1 mas.

We report in Table 6 for all our components (core, A, B, and C), for each epoch and frequency, the distance from the core, the position angle, the size, and the flux density for VLBA data; these flux values should be considered as rough estimates because, with different resolution and visibility coverage, there may be significant blending between compact components and diffuse emission. In particular, we expect a systematically lower flux with respect to the OVRO single-dish fluxes reported in our Fig. 1.

In Fig. 6, we plot the evolution of the components' separation from the core with time at the different frequencies: Our data are those between 2015 and 2016, while those in the 2019–2020 range come from the MOJAVE archive. The epochs of the two large γ-ray flares are marked with asterisks located at the core position. In Fig. 7, we report the positions in the plane of the sky, measured in mas from the core, of component B at different epochs and frequencies: this plot allows to check that the position angle of the motion is consistent with the jet axis, as apparent in Fig. 5. The presence of a quasi-stationary, more or less oscillating component at 1.4 mas from the core (our component C), is in agreement with previous studies on this radio source (see e.g. Roland et al. 2008), while components A and B can be regarded as new. Despite the difficulty in relating the components at different epochs with differing UV coverage and observing frequencies, our overall results are consistent with a scenario of a component B with a clear outward motion, with respect to the core component, along the jet direction, with a decreasing flux, and an additional component A separating from the core more slowly and with less reliably estimated positions.

We derived the proper motion of these components by means of a linear fit (see Fig. 8). We found that component A was moving with an apparent velocity v_app = (0.088 ± 0.011) mas yr^{-1}, corresponding to $(4.18 \pm 0.54)c$, and the estimated epoch of passage through the VLBI core was 2015.44 ± 0.44 (i.e. between 2015 January and

Table 4. Data from Gehrels et al. 2004 observations: the date (column 1), the MJD (column 2), the last digits of the observation identifier (column 3), the exposure time (column 4), the total counts (column 5), the net count rate (column 6), the photon index (column 7), the flux in the 0.3–10 kev range assuming a power-law spectrum, and the Galactic absorption (column 8).

Date	Date (MJD)	Obs id	Exp (s)	Counts	Count rate (counts s^{-1})	Photon index	Flux 10^{-12} (erg cm^{-2} s^{-1})	R_C (mag)
2009-06-07	54989.93	04	9337	710	0.075 ± 0.003	1.43 ± 0.06	4.08 ± 0.25	16.29
2009-10-13	55117.00	05	5097	269	0.052 ± 0.003	1.47 ± 0.10	3.05 ± 0.30	15.40
2011-02-23	55615.11	08	1274	100	0.078 ± 0.008	1.53 ± 0.17	4.36 ± 0.78	15.98
2011-02-23	55615.18	09	2547	162	0.063 ± 0.005	1.38 ± 0.14	3.81 ± 0.54	15.98
2011-05-05	55686.49	11	3696	141	0.038 ± 0.003	1.53 ± 0.15	2.81 ± 0.45	15.67
2011-05-06	55687.62	12	3654	202	0.055 ± 0.004	1.48 ± 0.12	3.00 ± 0.38	15.50
2011-05-07	55688.63	13	2392	142	0.059 ± 0.005	1.65 ± 0.13	2.68 ± 0.36	15.50
2011-05-08	55689.29	14	4335	261	0.059 ± 0.004	1.68 ± 0.10	2.58 ± 0.24	15.50
2011-05-09	55690.63	15	2270	81	0.035 ± 0.004	1.74 ± 0.24	2.36 ± 0.68	15.44
2012-01-04	55930.31	16	1394	61	0.043 ± 0.006	1.70 ± 0.30	2.49 ± 0.95	15.09
2012-01-08	55934.05	17	4350	223	0.051 ± 0.003	1.30 ± 0.11	2.90 ± 0.31	15.31
2015-08-23	57257.11	18	1743	120	0.068 ± 0.006	1.50 ± 0.15	3.43 ± 0.53	14.13
2015-09-09	57274.05	19	3911	264	0.067 ± 0.004	1.50 ± 0.09	3.29 ± 0.30	14.55

Table 5. VLBI observations epochs.

Array	Project	Date	Freq. (GHz)
EVN	EC057A	2016 Jun 14	22
VLBA	BC224A	2016 Sep 4	15, 43
VLBA	BC224B	2017 Mar 4	15, 43
EVN	EC057B	2017 Mar 8	22
VLBA	BC224C	2017 Nov 7	15, 43
EVN	EC057C	2018 Mar 14	22
VLBA	MOJAVE	2019 Aug 15	15
VLBA	MOJAVE	2019 Oct 8	15
VLBA	MOJAVE	2019 Nov 14	15
VLBA	MOJAVE	2019 Dec 15	15
VLBA	MOJAVE	2020 Jan 4	15
VLBA	MOJAVE	2020 Feb 28	15

Note. The array (column 1), the observation project name (column 2), the date (column 3), and the frequencies used (column 4).
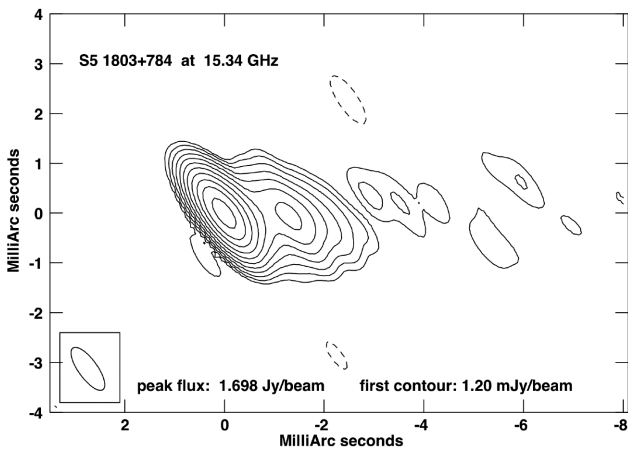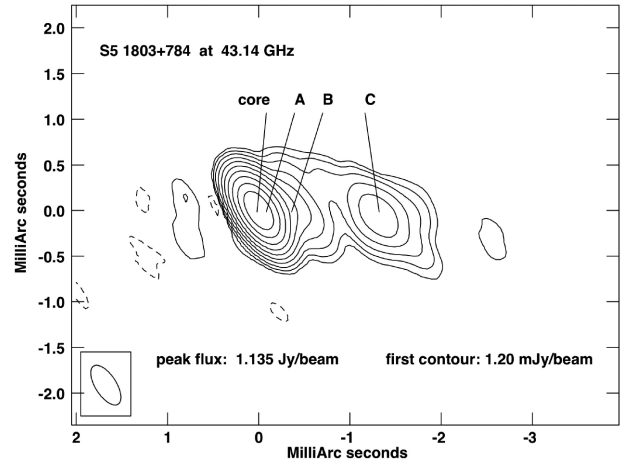

Figure 4. The radio map at 43 GHz on 2016 September 4 at 0.50×0.23 mas^2 resolution from VLBA. Contours increase by a factor of 2.

Figure 3. The radio map at 15 GHz on 2016 September 4 at 1.03×0.38 mas^2 resolution from VLBA. Contours increase by a factor of 2.
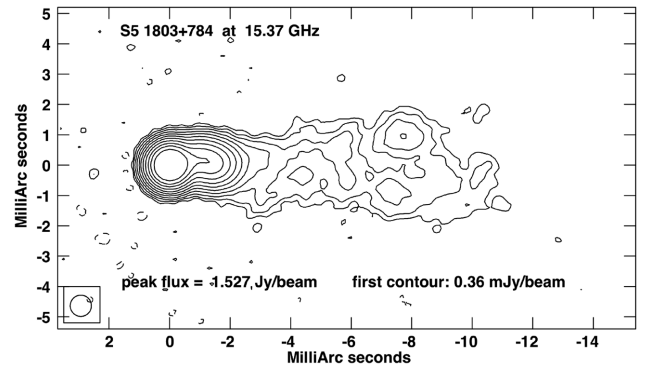

Figure 5. The radio map at 15 GHz at 0.77x0.65 mas^2 resolution recomputed by us using MOJAVE data of the years 2019–2020. Contours increase by a factor of 2.

November), consistent with the epoch of the flare on 2015 August 23.

On the other hand, component B was moving with v_app = (0.195 ± 0.014) mas yr^{-1}, corresponding to $(9.27 \pm 0.67)c$, and the estimated epoch of passage through the VLBI core was 2014.67 ± 0.28 (i.e. between 2014 May and December), consistent with the γ-ray flare on 2014 July 19.

Table 6. Position of radio components with respect to the core: the component nomenclature (column 1), year (column 2) distance from core (column 3), the position angle (column 4), the size (column 5), the flux density for VLBA (column 6), and frequency (column 7).

| Comp	Year	Dist. (mas)	PA (°)	Size (mas)	S (mJy)	Freq. (GHz)
core	2016.67			0.13	1740	15
core	2017.17			0.12	1610	15
core	2017.83			0.11	1720	15
core	2019.62			0.08	1660	15
core	2019.77			0.09	1530	15
core	2019.87			0.10	1470	15
core	2019.96			0.10	1370	15
core	2020.01			0.10	1410	15
core	2020.16			0.10	1430	15
core	2020.33			0.12	1520	15
A	2019.62	0.36	−79	0.27	181	15
A	2019.77	0.39	−78	0.29	159	15
A	2019.87	0.36	−76	0.41	206	15
A	2019.96	0.40	−80	0.28	147	15
A	2020.01	0.39	−79	0.32	176	15
A	2020.16	0.39	−76	0.39	158	15
A	2020.33	0.41	−80	0.39	146	15
B	2016.67	0.36	−87	0.32	254	15
B	2017.17	0.46	−79	0.41	264	15
B	2017.83	0.57	−77	0.51	183	15
B	2019.62	0.94	−76	0.31	148	15
B	2019.77	0.98	−77	0.33	150	15
B	2019.87	0.97	−76	0.33	147	15
B	2019.96	0.98	−76	0.33	131	15
B	2020.01	0.99	−77	0.35	139	15
B	2020.16	1.01	−76	0.32	126	15
B	2020.33	1.03	−77	0.31	102	15
C	2016.67	1.32	−92	0.52	184	15
C	2017.17	1.37	−93	0.62	213	15
C	2017.83	1.35	−91	0.77	251	15
C	2019.62	1.44	−88	0.31	130	15
C	2019.77	1.46	−88	0.36	138	15
C	2019.87	1.44	−87	0.36	157	15
C	2019.96	1.44	−88	0.39	167	15
C	2020.01	1.45	−88	0.38	171	15
C	2020.16	1.45	−88	0.42	190	15
C	2020.33	1.46	−88	0.45	197	15
core	2016.45			0.09	–	22
core	2017.19			0.09	–	22
core	2018.21			0.08	–	22
A	2016.45	0.16	−90	<.05	–	22
A	2017.19	0.22	−66	0.14	–	22
A	2018.21	0.27	−66	0.25	–	22
B	2016.45	0.31	−76	0.38	–	22
B	2017.19	0.51	−81	0.28	–	22
B	2018.21	0.88	−74	0.14	–	22
C	2016.45	1.27	−93	0.65	–	22
C	2017.19	1.43	−91	0.25	–	22
C	2018.21	1.29	−91	0.51	–	22
core	2016.67			0.06	1110	43
core	2017.17			0.05	992	43
core	2017.83			0.06	1110	43
A	2016.67	0.13	−46	0.09	144	43
A	2017.17	0.13	−69	0.17	115	43
A	2017.83	0.10	−126	0.14	80	43
B	2016.67	0.36	−85	0.29	64	43
B	2017.17	0.57	−78	0.36	61	43
B	2017.83	0.72	−79	0.43	83	43
C	2016.67	1.34	−92	0.37	83	43
C	2017.17	1.39	−93	0.21	55	43
C	2017.17	1.44	−92	0.45	90	43
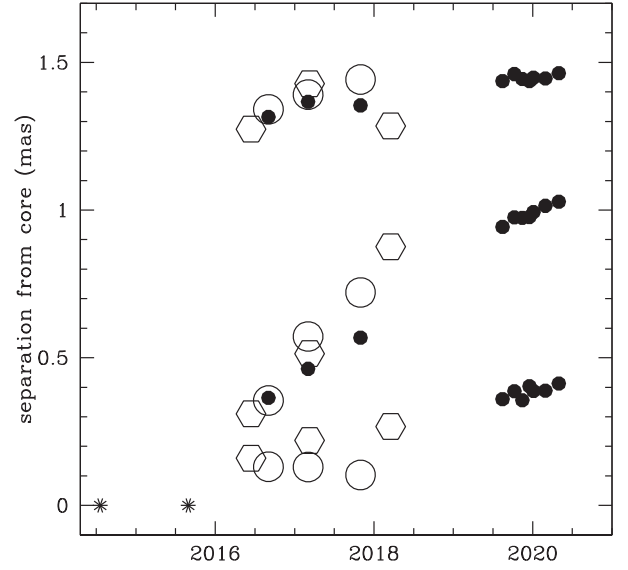
Figure 6. The separation between the core and the A (bottom), B (middle), and C (top) components as a function of time. *X*-axis in years, *y*-axis in mas; filled circles 15 GHz, open circles 43 GHz, and open hexagons 22 GHz. 2015 and 2016 data are from our VLBA and EVN observations, 2019-2020 data from the MOJAVE archive. Asterisks mark the epochs of the two large γ-ray flares.
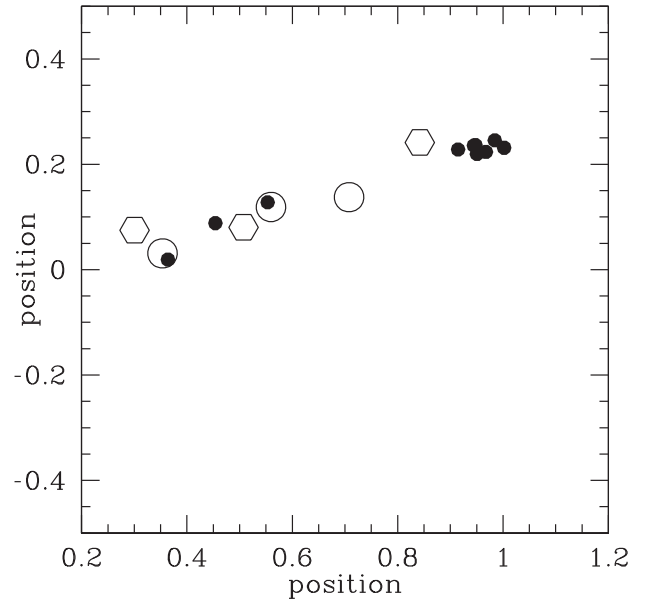

Figure 7. The position in the sky plane of the B component at different times with respect to the core at coordinates 0,0. North is up and east to the left. Units are mas for both axis, with 0,0 indicating the core component. Filled circles 15 GHz, open circles 43 GHz, and open hexagons 22 GHz.

The OVRO light curve (see Fig. 1) shows a local maximum around the beginning of 2014 November (MJD 56966), which may be related to the ejection of component B. However, the data points around this period are poorly sampled, preventing us from estimating the peak in a more accurate way. The same argument applies to the poorly sampled data points in 2015.
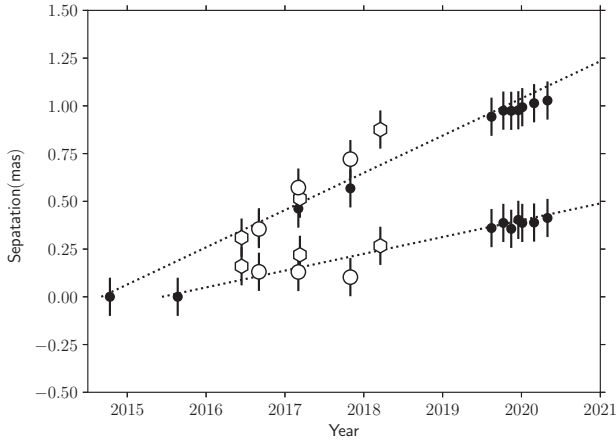
Figure 8. The separation between the core and the A (bottom), and B (top) components as a function of time. *X*-axis in years, *y*-axis in mas; the regression lines used to evaluate the ejection epochs of the two components are shown. For both components, extrapolation to $y = 0$ are compatible with the times of the two large γ-ray flares. Filled circles 15 GHz, open circles 43 GHz, and open hexagons 22 GHz.

4 DISCUSSION

Given the nature of the emission processes producing the spectral energy distribution of an LSP blazar such as S5 1803+784, some correlations are expected between the low- and the high-frequency components (see e.g. Röken et al. 2018 and references therein). We briefly discuss here the results of our monitoring.

4.1 Light curves comparison

The historic optical light curve of S5 1803+784 since 1996 (see Fig. 9) shows several flares, but without a well-defined period-icity: The time interval between consecutive flares is not constant, nor similar, as can be seen from Fig. 1 and Table 2 . A formal test using the Discrete Fourier Transform (DFT) for unevenly spaced data (Deeming 1975) also gave no dominant frequency.

In the 2008–2018 time interval, the source was monitored also by the *Fermi*-LAT and had two major flares with a large (factor ∼10) variability and a number of minor flares, characterized by a duration of about 60 d. The γ-ray light curve also does not show a clear periodicity. The main parameters of optical flares are given in Table 2; the γ-ray ones in Table 3. We briefly describe below the main flares. The first flare was followed by us a few days after the γ-ray flare of 2010 January 11 (MJD 55207; Donato 2010), so the actual optical peak value is unknown and only the falling slope was measured. A remarkably long high state occurred between MJD 55892 and 56040, peaking at $R = 14.4$ mag; the final part is undersampled, so the dimming slope is not well constrained. A shorter flare occurred around MJD 56206: the source was bright for about 60 d, but again the dimming phase is not well sampled: apparently no γ-ray increase was detected. A single bright optical point ($R = 14.5$ mag) was detected by MASTER on 56639, corresponding to a bright γ-ray level. A very bright flare occurred between MJD 56851 and 56899, apparently with a small precursor, and a brightening slope of 0.22 mag d^{-1}. The source remained in a high-activity state for about 45 d, with some oscillations. The actual end was not covered by the monitoring, so the flare was likely much longer. Around MJD 57099 we have just one photometric point, moderately bright (R

= 15.0 mag), from the Belgium Royal Observatory, corresponding to a high LAT flux. Another very bright flare started at MJD 57248, apparently again with a precursor, with a brightening slope of 0.11 mag d^{-1}, followed by an oscillating behaviour. The total duration was about 60 d. Two other minor optical flares occurred on 57348 and 57488, this last one without a γ-ray counterpart. A long bright state was detected between MJD 57719 and MJD 57747 peaking around $R = 14.4$ mag, with a corresponding high γ-ray flux. Overall, the bright states are typically long-lasting (tens of days) while the rising slopes show a range of values from 0.07 up to 0.22 mag d^{-1}. The dimming phases were not well recorded but apparently have flatter slopes. A fair qualitative correlation between the optical and γ-ray light curves is apparent from Fig. 1, although the lack of a γ-ray counterpart for the 'moderate' optical flares of 2012 October (MJD ∼ 56200) and 2016 April (MJD ∼ 57488) is evident.

For a better comparison, we report zoomed sections of the light curve centred on the last two major flares: Fig. 10 around MJD 56857, and Fig. 11 around MJD 57257. The upper panels show the light curves, while the lower panels show the discrete correlation function (DCF) binned at 3-d intervals. In the first flare, there is a substantial time coincidence of the γ-ray peak with the optical one. In the second flare, the delay of the optical peak with respect to the γ-ray one is just 3 d, corresponding to our time bin, so it is not significant.

No clear correlation is present between the 15-GHz total emission, as seen from the OVRO radio telescope, and the optical (and γ-ray) emission. This is in agreement with the previous finding by Nesci et al. (2002) based on the Medicina radio telescope at 8.4 GHz in the years 1996–2002.

Regarding the X-ray and optical emissions (see Table 4), the overall X-ray flux variation in the *Swift* pointings was a factor of ∼2, while the corresponding optical luminosities changed by a factor of ∼6. Overall, no clear correlation emerges from the data, suggesting that the X-ray emission is not directly linked to the optical photons. This is expected in an SSC scenario for an LSP BL Lac object, where the X-ray emission is considered to be produced by inverse Compton of relativistic electrons over photons of the radio/sub-mm range: The available X-ray data are however too sparse to look for a correlation between radio and X-ray emission.

We also searched for a correlation between X-ray and γ-ray fluxes for the available XRT pointings. To this purpose, we re-binned the LAT data on 10-d windows centred on the XRT epochs, and summed the XRT data taken at a few days distance: The results are shown in Fig. 12. The range of flux variation in the γ-ray band was about a factor of 10, against a factor of only ∼2 for X-rays. In the SSC scenario, the X-ray emission is the low-energy tail of the inverse-Compton energy distribution, which is peaked at γ-ray frequencies. One may therefore expect that the X-ray flux is larger for larger γ-ray flux. Unfortunately, we have simultaneous XRT data only during the 2015 γ-ray flare, while no data are available for the 2014 one. All the other observations were performed with the source in a nearly quiescent state. Our data in Fig. 12 suggest that, in a quiescent state, there is, if any, an anticorrelation between X-ray and γ-ray fluxes, i.e. larger X-ray flux for lower γ-ray flux.

For S5 1803+784, the position of the γ-ray peak is around 10^{22} Hz, somewhat below the energy band where the LAT instrument is most sensitive, and therefore not well measured. The LAT data trace the falling branch of the emission, which is expected to be much more variable than the X-ray branch. Therefore, the detection of a
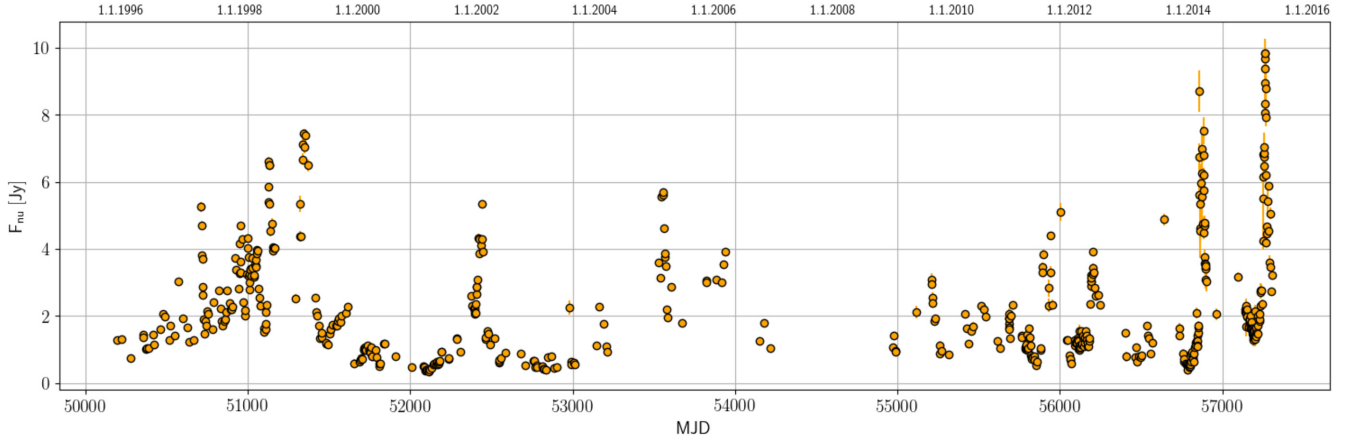
Figure 9. The historic R_C light curve of S5 1803+784 from 1996 to 2018.
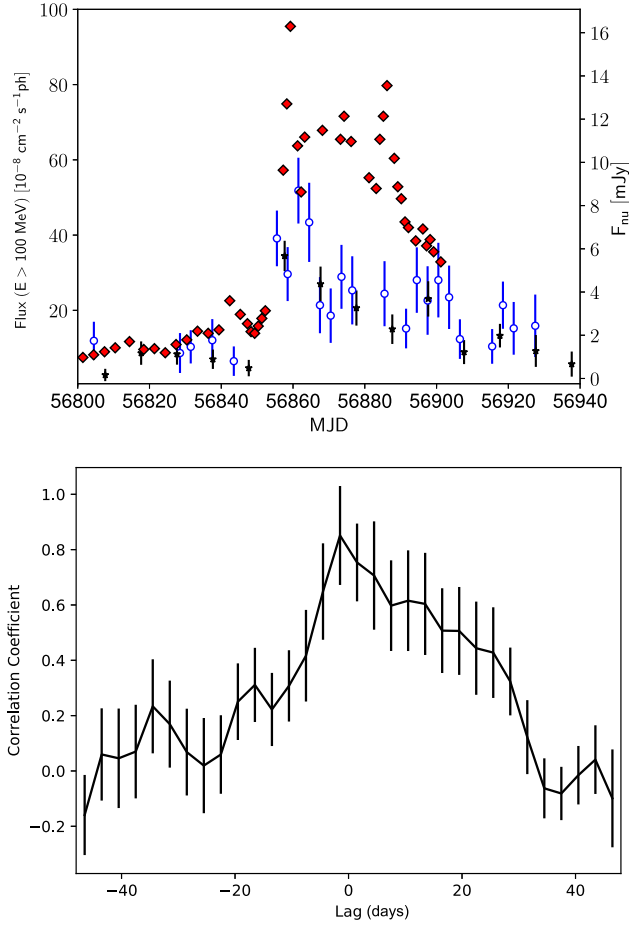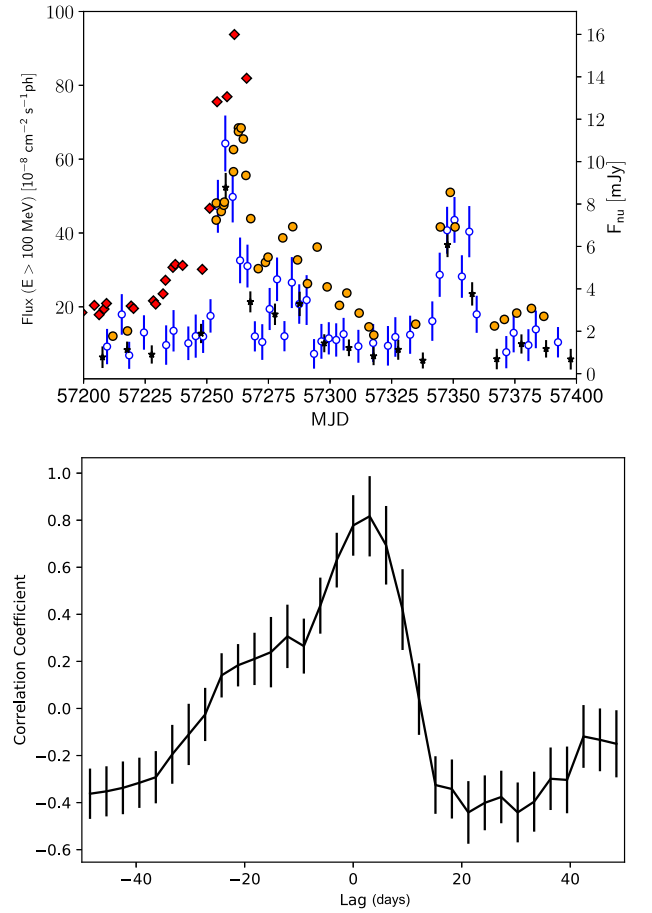

Figure 10. Top panel: the γ-ray light curve in the 0.1–300 GeV energy range, binned at 1- and 3-d intervals shown in blue open circle and black star respectively, for the flare around MJD 56857. The upper limit data points are not displayed. The optical light curve is over-plotted for comparison, with the same colour codes of Fig. 1. Bottom panel: the DCF between γ-ray and optical LC during the first flaring activity: X-axis is in days.

Figure 11. Top panel: the γ-ray light curve in the 0.1–300 GeV energy range, binned at 1- and 3-d intervals shown in blue and open circle and black star respectively, for the flare around MJD 57257. The upper limits data points are not displayed. The optical light curve is overplotted for comparison, with the same colour codes of Fig. 1. Bottom panel: the DCF between γ-ray and optical LC during the second flaring activity: X-axis is in days. Positive values indicate γ-rays leading.
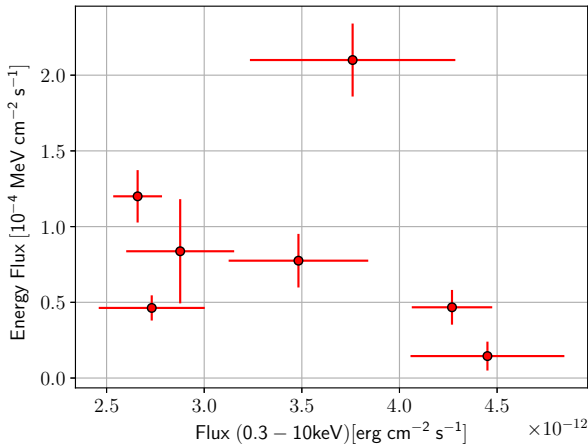
Figure 12. The X-ray *versus* γ-ray flux for S5 1803+784 from nearly simultaneous *Swift*-XRT and *Fermi*-LAT data.

correlation might require a higher accuracy in the flux measurements for both energy ranges.

4.2 Spectral slopes

The optical and UV spectral slopes showed very small variations during our monitoring. The near constancy of the optical and UV colour indexes allowed us to more densely build our light curve, as discussed in Sections 2.1 and 2.4.

The γ-ray spectrum of the source can be well fitted by a simple power law $N_\nu = A\nu^{-a}$, where N is the number of photons for a given frequency: the photon index a has an average value 2.26 ± 0.02, which is the transition value between FSRQs and LSP BL Lacs detected by *Fermi*-LAT (Ajello et al. 2020).

We looked for a possible correlation of the photon index with the source luminosity. Indeed, we found a monotonic increase of the spectral index with flux, considering only observations with TS≥25, while this trend disappeared considering all the observations including also the less significance data points.

We explored therefore the possibility of a systematic effect in the computation of the spectral index at low flux levels, as is the case of our 10-d time bins. We performed extensive simulations giving as input to the *Fermi*-LAT software synthetic spectra with power-law indices of 1.5, 2.0, and 2.5, and total fluxes varying as in our source, with the same background as in our real data. Indeed, we found that below a flux level corresponding to about 1.0×10^{-7} photons cm^{-2} s^{-1}, the simulated spectra pointed out a systematic underestimation of power-law index value. Therefore the apparent trend found in our observations of S5 1803+784 is likely spurious.

Finally, we built the average spectrum of the quiescent state, summing all the observations with flux below 2.3×10^{-7} photons cm^{-2} s^{-1} (our flaring level defined in Section 2.3), and the average spectrum of the active state, summing all the observations above that level. Both spectra were well described by a power law with the same spectral index (2.22 ± 0.01 for the low state and 2.21 ± 0.02 for the high state).

4.3 Optical spectrum

Besides being useful to measure the redshift, and then the distance of the source, the emission lines in a blazar can help us to understand

where they are formed: close to the central engine, before the jet is fully developed, or beyond the jet, illuminated by its radiation. In the first case, if they are excited by the photons coming from the accretion disc, their luminosity should remain unchanged and their EW would drop significantly during a flare, which increases only the continuum emission. In the second case, the emission lines are excited by the jet and their luminosity should follow the jet intensity, so their EW should remain somewhat constant during a flare.

Our spectrum was taken near a flare peak, with the continuum emission a factor of ∼9 larger than in 1996 and 2018, when the Mg II emission line was evident. If the flux of the emission line were constant, it would be completely undetectable in our spectrum, which is what we actually found. We argue therefore that the emission-line region is not excited by the radiation of the jet and is likely close to the central engine.

5 CONCLUSIONS

No definite periodicity was detected in our optical and γ-ray light curves of S5 1803+784. In recent studies (Kun et al. 2018), a period of about 8 years for the precession of the relativistic jet has been claimed, based on the analysis of VLBI images. From the data that we collected, there is no clear optical or γ-ray counterpart of this phenomenon.

Regarding the spectral variability, the optical (*V*, *R*, *I*) spectral index was rather constant during our monitoring, regardless of the source optical luminosity, and very similar to that shown by the source in the previous twelve years (Nesci et al. 2002). The X-ray spectral index showed no evidence of hardening at higher fluxes. Also, the γ-ray photon spectral index showed no significant variations correlated with the luminosity, in contrast to 'softer when brighter' behaviour observed in some cases (e.g PKS 2155−304, Foschini 2010 and PKS 0219−164, Bhatta 2017), or a 'harder when brighter' behaviour found by Foschini et al. 2013 in the case of PKS 1510−089. The absence of spectral evolution as a function of the luminosity could be related to the location of the γ-ray emission region in the flaring state beyond the emission-line region. However, being a BL Lacertae object, S5 1803+78 is characterized by extremely weak emission lines, with a small size of the emission-line region that does not induce a strong absorption of higher energy γ-ray photons and a steepening of the spectral index in flaring phase (Costamante et al. 2018).

An optical spectrum taken during the maximum of the 2015 flare did not show the emission line of Mg II 2790 Å, present when the source was in a much fainter state: This is expected if the emission line is generated in a volume closer to the core than to the jet emitting the synchrotron radiation, and therefore is not excited by the jet radiation.

We found no correlation between X-ray and optical fluxes: this is expected if the X-ray flux comes from the low-energy tail of an Inverse-Compton emission process, while the optical emission comes from the high-frequency tail of the synchrotron radiation. In contrast, the γ-ray emission showed a fair correlation with the optical one, except in the case of some minor optical flares when no γ-ray enhancements were detected. In the two major flares, which have a better time sampling, the γ-ray flux rises simultaneously with the optical one but falls a bit earlier, producing a narrower peak. The optical/γ-ray flux ratio is expected to be rather constant in an SSC model: Actually, the flux ratios listed in column 5 of Table 3 show a mildly increasing trend with time, from less than 1 in 2009 to about 3 in 2015, with correlation coefficient 0.84. The

morphology of the source, traced at mas resolution by the VLBI radio observations covering a span of several years after the large γ-ray-optical flares, shows a clearly detected component moving outwards after the first flare, slowly decreasing in flux. Another similar component appears to have been generated by the second flare, although with a smaller apparent velocity in the plane of the sky. This finding strongly supports a causal connection between the mechanisms producing the high-energy and the radio-band radiation in blazars.

DATA AVAILABILITY

All the data not already included in the tables are available from the authors on request.

REFERENCES

Abdo A. A et al., 2009, ApJ, 700, 597
Abdollahi S . et al., 2020, ApJS, 247, 33
Ajello M . et al., 2020, ApJ, 892, 105
Atwood W. B et al., 2009, ApJ, 697, 1071
Atwood W . et al., 2013, preprint (arXiv:1303.3514)
Bhatta G., 2017, ApJ, 847, 7
Biermann P et al., 1981, ApJ, 247, L53
Britzen S et al., 2010, A&A, 511, A57
Chiaberge M., Celotti A., Capetti A., Ghisellini G., 2000, A&A, 358, 104
Costamante L., Cutini S., Tosti G., Antolini E., Tramacere A., 2018, MNRAS, 477, 4749
Deeming T. J., 1975, Ap&SS, 36, 137
Donato D., 2010, Astron. Telegram, 2386
Drake A. J et al., 2009, ApJ, 696, 870
Foschini L., 2010, Astron. Telegram, 2947
Foschini L., Bonnoli G., Ghisellini G., Tagliaferri G., Tavecchio F., Stamerra A., 2013, A&A, 555, A138
Gehrels N et al., 2004, ApJ, 611, 1005
Helene O., 1983, Nucl. Instrum. Methods Phys. Rev., 212, 319
Kun E., Karouzos M., Gabányi K. É., Britzen S., Kurtanidze O. M., Gergely L. Á., 2018, MNRAS, 478, 359
Lampens P., van Cauteren P., 2015, Astron. Telegram, 7988
Lawrence C. R., Zucker J. R., Readhead A. C. S., Unwin S. C., Pearson T. J., Xu W., 1996, ApJS, 107, 541
Li W., Filippenko A. V., Chornock R., Jha S., 2003, PASP, 115, 844
Lipunov V . et al., 2010, Adv. Astron., 2010, 349171
Lister M. L., Aller M. F., Aller H. D., Hodge M. A., Homan D. C., Kovalev Y. Y., Pushkarev A. B., Savolainen T., 2018, ApJS, 234, 12
Mattox J. R et al., 1996, ApJ, 461, 396
Monet D. G et al., 2003, AJ, 125, 984
Nesci R., Massaro E., Maesano M., Montagni F., Sclavi S., Venturi T., Dallacasa D., D'Alessio F., 2002, AJ, 124, 53
Nesci R., Maselli A., Montagni F., Sclavi S., 2012, Acta Polytech., 52, 39
Padovani P., Giommi P., 1995, ApJ, 444, 567
Paiano S., Falomo R., Treves A., Scarpa R., 2020, MNRAS, 497, 94
Rector T. A., Stocke J. T., 2001, AJ, 122, 565
Richards J. L et al., 2011, ApJS, 194, 29
Röken C., Schuppan F., Proksch K., Schöneberg S., 2018, A&A, 616, A172
Roland J., Britzen S., Kudryavtseva N. A., Witzel A., Karouzos M., 2008, A&A, 483, 125

This paper has been typeset from a TEX/LATEX file prepared by the author.